ACS APPLIED MATERIALS & INTERFACES

Research Article

www.acsami.org

Interconnected Network of MnO_2 Nanowires with a "Cocoonlike" Morphology: Redox Couple-Mediated Performance Enhancement in Symmetric Aqueous Supercapacitor

Sandipan Maiti, Atin Pramanik, and Sourindra Mahanty*

Fuel Cell & Battery Division, Central Glass & Ceramic Research Institute, Council of Scientific and Industrial Research, Kolkata 700032, India

Council of Scientific and Industrial Research−Network of Institutes for Solar Energy, New Delhi, India

Supporting Information

ABSTRACT: Low electronic conductivity and slow faradic processes limit the performance of MnO_2 as an electrochemical pseudocapacitor with respect to cycling and power density. Herein, we report preparation of single-phase α-MnO_2, composed of an interconnected nanowire network with "cocoonlike" morphology, and its application as electrode in a symmetric aqueous supercapacitor. Increased "effective" surface area, coexistence of micropores and mesopores, and enhanced electron transport in these nanowire networks result in a specific pseudocapacitance (C_S) of 775 $F{\cdot}g^{-1}$ in 3 M KOH, derived from cyclic voltammetry in the potential window of −1 to +1 V at a scan rate of 2 $mV{\cdot}s^{-1}$, the highest reported for two-electrode symmetric configuration. Furthermore, introduction of $K_4Fe(CN)_6$ as a redox-active additive to KOH results in ∼7 times increase in energy density at a power density of ∼6000 $W{\cdot}kg^{-1}$. The presence of the $Fe(CN)_6^{4-}/Fe(CN)_6^{3-}$ redox couple provides an electron buffer source compensating for the slow faradic reactions. The results demonstrate that this simple approach might be an effective way to enhance the redox kinetics and reversibility of transition metal oxide-based pseudocapacitors.

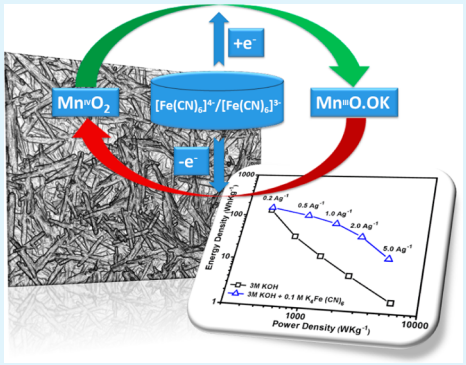

KEYWORDS: *energy storage, electrochemical pseudocapacitor, MnO_2 nanowires, hydrothermal synthesis, $Fe(CN)_6^{4-}/Fe(CN)_6^{3-}$ redox couple*

1. INTRODUCTION

Electrochemical supercapacitors (EC), due to a number of favorable features such as high power density, high energy efficiency, and long cycle life, are the most promising energy storage devices that can bridge the power/energy gap between batteries and conventional dielectric capacitors.[1−3] However, the energy density of ECs is about an order of magnitude lower than that of batteries. Nonetheless, ECs have found application in mobile electronics, backup power supplies, and electric vehicles.[4,5] Charge storage in EC is mainly based on two principles: (i) ion accumulation on electric double layer (electric double-layer capacitor, EDLC) and (ii) surface or near-surface faradic redox reactions (pseudocapacitor).[6,7] Transition metal oxides are considered to be good electrode materials for their intrinsic high pseudocapacitance. RuO_2 shows probably the best supercapacitive properties,[7] but high price and toxic properties limit its practical application. In recent years, MnO_2 has emerged as a cheaper and ecologically benign alternative having a reasonably high theoretical pseudocapacitance (1109.9 $F{\cdot}g^{-1}$) and good chemical stability.[8−11] But due to its low intrinsic conductivity (10^{-5}−10^{-6} $S{\cdot}cm^{-1}$), the capacitance of MnO_2 could not be entirely gained in most cases. To practically approach the theoretical capacitance, MnO_2 should be of monolayer thickness so that the entire MnO_2 surface could be utilized, and also, the electron and ion transport should be extremely fast. Thus, in view of the importance of particle size and morphology, research efforts have been focused on synthesizing MnO_2 nanoparticles and/or organizing them into three-dimensional nanostructures such as nanowires,[12] nanorods,[13] nanobelts,[14] nanosheets,[15] hierarchical spheres,[16] sea urchin-like hollow spheres,[17] octahedral molecular sieves,[18], etc. It is found that high surface area and optimized ion transport both contribute to the electrochemical performance of MnO_2 nanostructures, and specific capacitance values of 279,[12] ∼180−210,[13] and ∼140−160[15] $F{\cdot}g^{-1}$ have been reported. Again, to overcome the conductivity issue, composite materials like MnO_2/graphene,[19−23] MnO_2/carbon nanotube (CNT),[24−26] and conductive polymer-based MnO_2−polyaniline (PANI),[27] MnO_2−poly(3,4-ethylenedioxythiophene) (PEDOT),[28] etc., have also been investigated, and capacitance as high as 1068 $F{\cdot}g^{-1}$ has been realized.[28] Recently, Liu et al.[29] reported the development of MnO_2/porous carbon microspheres with a partially graphitic structure for high-performance supercapacitor electrodes, and they achieved

Received: May 1, 2014
Accepted: June 16, 2014
Published: June 16, 2014

excellent results under high current density. Developing core−shell nanowires[30] and nanocables[31] also leads to high capacitance values, alleviating the conductivity problem to a large extent. Sandwich configuration of Mn−MnO_2,[32] and noble metal-loaded MnO_2[33] also showed promising results. Most of the supercapacitor studies have been conducted in three-electrode configuration. Two-electrode symmetric configuration, though it might be more convenient from the practical application point of view, generally yields lower capacitance values. In two-electrode configuration, Ma et al.[34] have reported a high capacitance of 266.6 $F{\cdot}g^{-1}$ in 1 M Na_2SO_4 at a current density of 0.1 $A{\cdot}g^{-1}$ for hierarchical MnO_2 hollow spheres. Wang et al.[35] have obtained capacitance of 198.1 $F{\cdot}g^{-1}$ in 1 M Na_2SO_4 and a still higher value of 401.4 $F{\cdot}g^{-1}$ in a relatively higher concentration of alkaline electrolyte, 9 M KOH, which leads to corrosion of the current collector. Recently, Xia et al.[36] have shown that synergic combination of designer core−shell structure (Co_3O_4 core and PEDOT/MnO_2 shell) leads to an enhanced rate capability and structural stability. Despite all these advances, a simple and effective strategy is still needed to overcome the gradual decrease in pseudocapacitance of MnO_2 upon longer cycling and with increasing current density. Issues of low conductivity of the material and slow electron transfer rate of redox (faradic) reactions remain the central focus of current research for developing high-performance MnO_2-based pseudocapacitors for energy storage.

To address the above issues, we have undertaken a two-way approach to improve the power density, which is closely related to the reaction kinetics of the redox processes and efficient transfer of charge: (1) Creation of an interconnecting network of MnO_2 nanowires with coexistence of micropores and mesopores. This would ensure unhindered access of electrolyte to every possible surface of the active material and shorten the transport path of ionic species. At the same time, it would facilitate electron transport through the available interconnecting conduction pathways. (2) Addition of a fast redox-active couple that would act as an electron buffer to compensate for the slow nature of the faradic reactions. As pseudocapacitance originates from surface or near-surface reversible redox reactions of the active material, it is logical to expect that this phenomenon would be accelerated by electrochemically reversible redox additives to the electrolyte, where two electrochemical redox reactions would occur simultaneously at the surface layer of active material and in the electrolyte, complementing each other at the electrode/electrolyte interface. Until now, to the best of our knowledge, there is no report available on the effect of redox-active electrolyte additives on the supercapacitive performance of MnO_2, though a couple of recent works have shown that the capacitive performance of Co−Al layered double hydroxide system or $Co(OH)_2$/graphene nanosheet is improved by adding hexacyanoferrate-(II) and -(III) into 1 M KOH.[37,38] Thus, in this work, we have investigated the performance of hydrothermally synthesized interconnected α-MnO_2 nanowires as symmetric supercapacitors by adding electrochemically reversible $Fe(CN)_6^{4-}$/$Fe(CN)_6^{3-}$ couple into 3 M KOH, and we have shown that indeed a significant enhancement in both energy density and power density could be achieved together with good cyclability by adopting this simple strategy.

1.1. Specific Capacitance, Power Density, and Energy Density of a Symmetric Capacitor. A symmetric capacitor can be considered as a combination of two electrode/electrolyte interfaces acting in series, and the overall capacitance of the cell (C_{cell}) can be expressed as[39−41]

$$1/C_{cell} = 1/C_{electrode\_1} + 1/C_{electrode\_2} \quad (1)$$

Thus, for a symmetric capacitor, if the active mass of both electrodes is the same, the capacitance of a single electrode would be

$$C_{electrode} = 2C_{cell} \quad (2)$$

The specific capacitance (C_s) of an electrode in a symmetric cell can be experimentally obtained by cyclic voltammetry (CV) or galvanostatic charge−discharge measurements via the following relationship:[42]

$$C_s = 4I/M(\Delta V/\Delta t) \quad (3)$$

where I is the discharge current, M is the sum of active mass of both electrodes, and $\Delta V/\Delta t$ is the potential scan rate (CV) or slope of the discharge curve (charge−discharge). If the active mass of both electrodes is the same, then eq 3 can be expressed as

$$C_s = 2I/m(\Delta V/\Delta t) \quad (4)$$

where m is the mass of a single electrode.

Accordingly, the energy density (E) and power density (P) values can be calculated from the relationship

$$E = {}^1\!/_2\, C_s(\Delta V)^2 \quad (5)$$

$$P = E/t = {}^1\!/_2\, I\Delta V \quad (6)$$

2. EXPERIMENTAL SECTION

2.1. Synthesis of Nanostructured MnO_2. All chemicals were used as received without further purification. Ultrapure water was used in all experiments and was obtained from a three-stage Millipore Milli-Q (Merck, Germany) purification system.

In a typical synthesis, MnO_2 nanowires were prepared by hydrothermal method under acidic conditions. First 3.56 g (0.25 mol) of $MnSO_4{\cdot}H_2O$ (99+%, Acros Organics, India) was dissolved in 84 mL of deionized water, and then 1.2 mL of concentrated H_2SO_4 was added dropwise (solution A). Then 2.2 g (0.25 mol) of $KMnO_4$ (99+%, Merck, Germany) dissolved in 56 mL of deionized water was added to solution A dropwise with constant stirring. The mixture was then transferred to a 160 mL Teflon-lined autoclave. The autoclave was sealed and maintained at 120 °C for 12 h. After that it was allowed to cool to room temperature. The black mass obtained was centrifuged and washed several times with deionized water and absolute alcohol to remove residual reactants. Finally, the product was dried at 110 °C for 12 h in an air oven.

2.2. Material Characterization. X-ray powder diffractograms (XRD) were recorded in the 2θ range 10°−80° at a slow scanning rate of $1^\circ{\cdot}min^{-1}$ by an X-ray diffractometer (Philips X'Pert, The Netherlands) with Cu Kα radiation at 40 kV and 40 mA. Phase analyses of the X-ray diffraction profiles were carried out with the PANalytical HighscorePlus program. Fourier transform infrared spectroscopy (FT-IR) was carried out to identify the characteristic bands in the wavenumber range from 4000 to 400 cm^{-1} by use of a Bomen infrared spectrophotometer in transmission mode through KBr (spectroscopy grade) disc formation. Synthesized α-MnO_2 nanowires have been further characterized by a Renishaw In Via Reflex micro Raman spectrometer using the 488 nm line of an Ar^+ ion laser for excitation in the range 200−1000 cm^{-1}. Microstructural studies were carried out by a field emission scanning electron microscope (FESEM; Zeiss Supra 35, Germany). High-resolution transmission electron microscopy (HRTEM) and selected area electron diffraction (SAED) studies were carried out on a Tecnai G2 30ST (FEI) microscope with

an accelerating voltage of 300 kV. Thermogravimetric analysis (TGA) of the powder sample was done under argon flow at a heating rate of 10 °C·min^{-1} on a simultaneous thermal analyzer (STA 449F, Netzsch, Germany). Nitrogen adsorption−desorption measurements were carried out on a Quantachrome Autosorb surface analyzer at 77.3 K. The sample was degassed under vacuum at 200 °C for 3 h prior to measurement. The specific surface area of MnO_2 was measured by nitrogen gas absorption through the Brunauer−Emmett−Teller (BET) method. Pore size distribution was estimated from desorption isotherm by the Barrett−Joyner−Halenda (BJH) method. Pore volume was determined from the amount of nitrogen adsorbed at P/P_0 = 0.98.

2.3. Electrochemical Measurements. The working electrodes were fabricated by mixing 80 wt % active material (synthesized MnO_2), 15 wt % SuperP carbon, and 5 wt % poly(tetrafluoroethylene) (PTFE) in isopropyl alcohol (IPA) to form a viscous paste. The paste was drop-cast on circular discs of nickel foil (thickness ∼50 μm) with a diameter of 15 mm. The electrodes were heated at 110 °C for 6 h in a vacuum oven to evaporate the residual solvent. Two-electrode symmetric supercapacitors were assembled with these electrodes in 2032 coin cells by use of a microporous separator (thickness ∼10 μm) of 19 mm diameter. Mass of the active material on electrodes was around 2 mg. The accuracy of electronic balance used is 0.01 mg (MS105DU, Mettler Toledo). Cyclic voltammetry (CV), galvanostatic charge−discharge, and electrochemical impedance spectroscopy (EIS) were carried out on a galvanostat−potentiostat (PGSTAT 300N, Autolab, The Netherlands). CVs were measured at different scan rates of 2, 5, 10, 20, 50, and 100 mV·s^{-1} in two different potential windows of −1 to +1 V and 0 to 1 V. Galvanostatic charge−discharge measurements were carried out at current densities of 0.2, 0.5, 1, 2, and 5 A·g^{-1} in the same potential windows; that is, both −1.0 to 1.0 V and 0 to 1 V. EIS measurements were carried out in the frequency range 0.1−100 kHz at open circuit potential with alternating current (ac) amplitude of 10 mV, and the obtained data were fitted to an equivalent circuit model by use of NOVA 1.9 software.

3. RESULTS AND DISCUSSION

3.1. Structure, Morphology, and Thermal Stability of Synthesized MnO_2 Nanowires. To determine the crystalline phase, X-ray diffraction measurements were conducted (Figure 1a). All the observed peaks could be indexed to a tetragonal phase (space group *I*4/*m*) of α-MnO_2 (JCPDS data file 00-044-0141). The calculated lattice parameters ($a = b$ = 9.785 Å and c = 2.863 Å) are in good agreement with reported values.[18] Absence of any additional diffraction peak indicates that the synthesized material is single-phase tetragonal MnO_2 of high purity. The FT-IR spectrum, shown in Figure 1b, also supports the observations in XRD. The sharp peaks appearing at 524 and 465 cm^{-1} are characteristic vibrations of Mn−O bonds, and the weak bands at 1408 and 717 cm^{-1} are characteristic vibrations of the O−Mn−O bonding in α-MnO_2.[43,44] The peaks observed around 3436 and 1643 cm^{-1} correspond to the stretching and bending mode of H−O−H vibration of absorbed water molecule, and the weak band centered at 1114 cm^{-1} can be assigned to vibration of the hydroxyl groups. In the Raman spectrum of synthesized α-MnO_2 nanowires (Figure 1c), the observed band at 578 cm^{-1} is the signature of Mn−O lattice vibration in α-MnO_2. The other band, observed at 630 cm^{-1}, corresponds to Mn−O lattice vibration in Mn_3O_4, possibly formed during spectral acquisition because of the local heating of α-MnO_2 nanowires.[45,46] The synthesized α-MnO_2 nanowires are thermally stable up to 500 °C, above which detachment of lattice oxygen occurs,[47] as found by thermogravimetric analysis (Figure S1, Supporting Information).

Morphology of the synthesized α-MnO_2 was investigated by FESEM. A low-magnification micrograph (Figure 2a,b) reveals

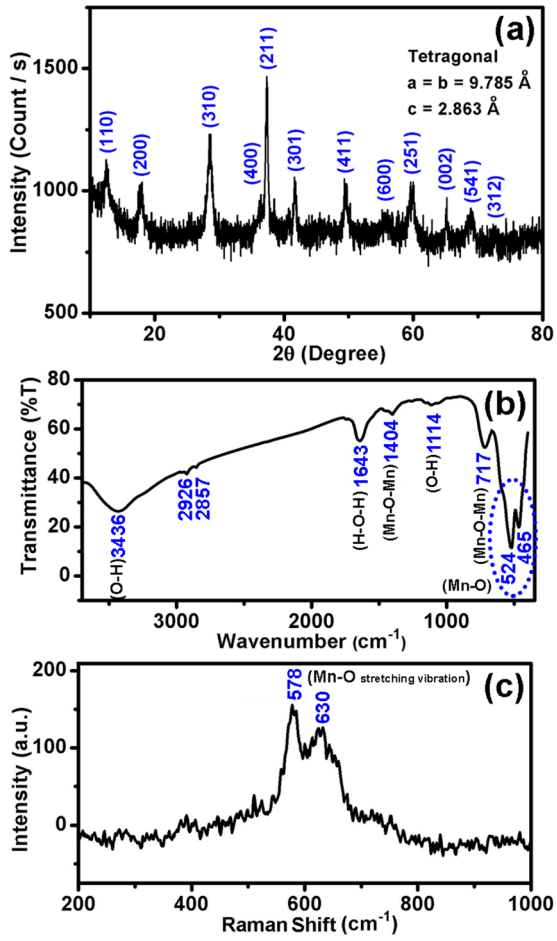

Figure 1. Structural characterization of synthesized α-MnO_2 nanowires: (a) X-ray diffractogram, (b) FT-IR spectrum, and (c) Raman spectrum.

formation of a matrix of criss-cross intersecting nanowire net in which "cocoon"-shaped spherical balls with varying sizes of 1−8 μm are evenly dispersed. From high-magnification FESEM (Figure 2c,d) and TEM (Figure 2e) images, it is clearly found that both the cocoonlike structures and the nanowire net underneath are composed of many distinct interconnected MnO_2 nanowires with an average diameter of 20 nm and an average length of 0.8 μm (Figure 2e inset). Absence of any contrast between the edges and the tips of the nanowires indicates these are solid nanowires rather than hollow nanotubes.

The hydrothermal reaction of $KMnO_4$ and $MnSO_4$ occurs via reduction of MnO_4^- intermediate with an overall redox reaction:

$$KMn^{VII}O_4 + Mn^{II}SO_4 \rightarrow Mn^{IV}O_2 + K_2SO_4 + H_2SO_4 \quad (7)$$

Nucleation and growth kinetics primarily dictate the architecture of hierarchically ordered nanostructures. The redox potential of MnO_4^-/Mn^{4+} (1.70 V) being slightly higher than Mn^{4+}/Mn^{2+} (1.23 V), the growth process is mild and proceeds at a slow rate. Moreover, the presence of H_2SO_4 in the reaction medium further inhibits the growth rate by common ion effect. On the other hand, the nucleation process is primarily controlled by the reaction temperature. A relatively lower temperature of 120 °C renders the nucleation process

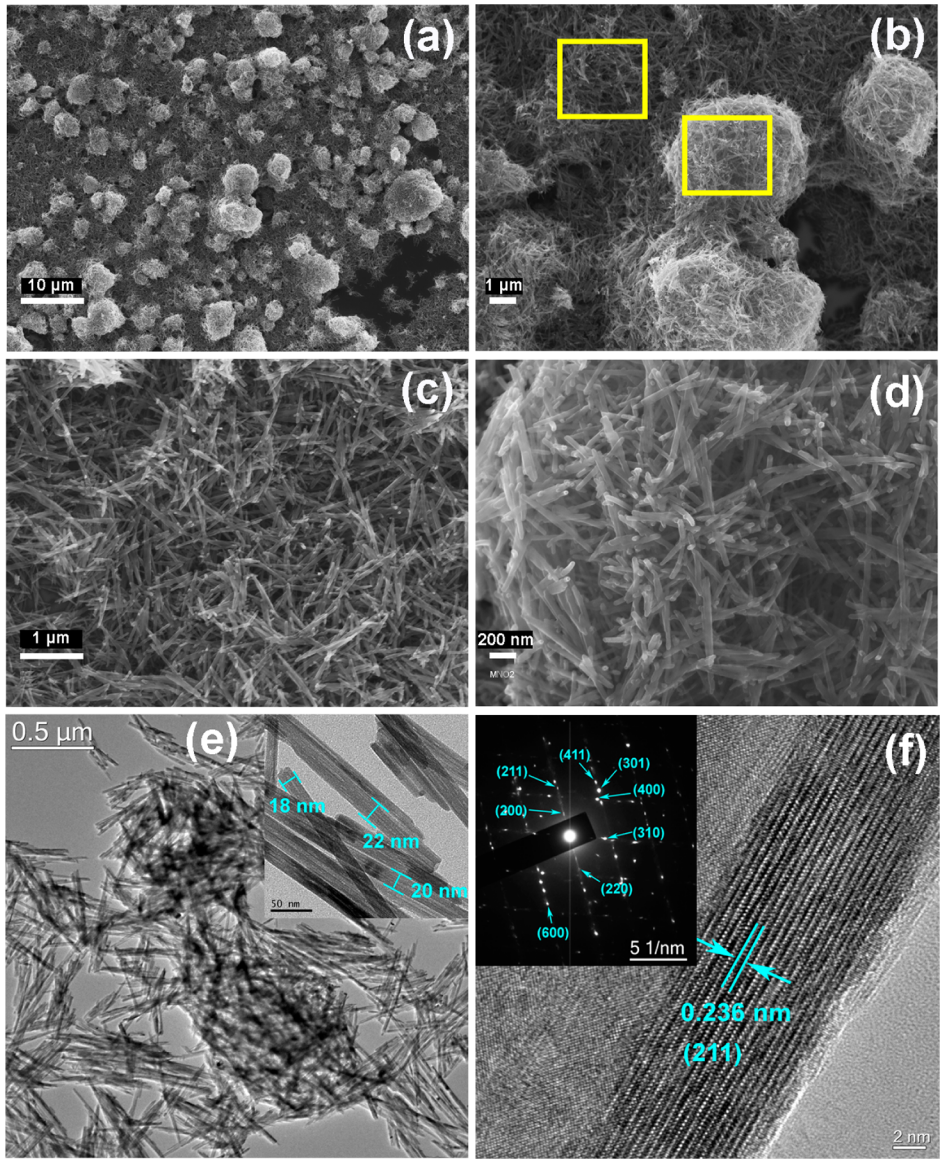

Figure 2. Morphological characterization of synthesized α-MnO_2 nanowires. (a, b) Distribution of "cocoonlike" features within a matrix of nanowire net. (c, d) High-magnification FESEM micrographs corresponding to the marked areas in panel b. (e) TEM and (f) HRTEM images. (Insets) SAED patterns.

slow, and the interfacial tension of the nanocrystals may induce criss-cross dendritic growth into a self-organized assembly of nanowire bundles with a cocoonlike shape with bimodal pore size. The structure of manganese dioxide is governed by the type of linkage and organization of MnO_6 octahedra.[48] The width of the lattice fringes (0.236 nm), as observed in the HRTEM image (Figure 2f), corresponding to the (211) plane, equals the pore size of 2 × 2 edge-shared MnO_6 octahedra having one-dimensional (1D) channels, characteristic feature of α-MnO_2. Furthermore, the SAED pattern (Figure 2f, inset) taken from a single nanowire indicates the single-crystalline nature of the individual nanowires.

Surface area, pore size, and their distribution are important parameters for the performance of a supercapacitor electrode. The N_2 adsorption−desorption isotherms and pore size distribution plot of synthesized MnO_2 nanowires are presented in Figure 3. The configuration of the plot displays a typical type II/IV isotherm with a discrete hysteresis loop starting from P/P_0 = 0.4. BET surface area measurement reveals that these

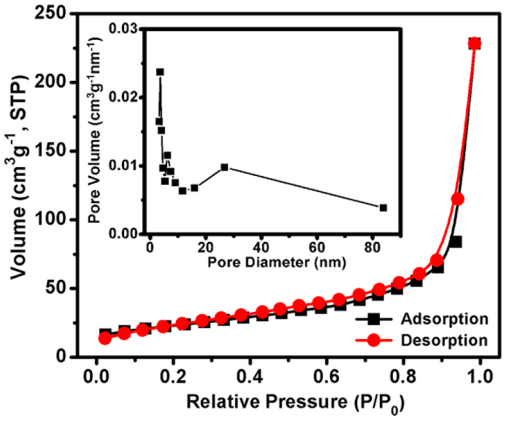

Figure 3. N_2 adsorption−desorption isotherm of synthesized α-MnO_2 nanowires. (Inset) Pore size distribution.

synthesized nanowires have a gravimetric surface area of 80.3 $m^2 \cdot g^{-1}$. The pore size distribution, calculated from the adsorption part of the nitrogen sorption isotherm, reveals a broad size distribution in the range of 3−85 nm with an average pore size of ∼4 nm. Coexistence of mesopores and micropores in these nanowires with a cocoonlike morphology could effectively solve the problem of agglomeration (thus increasing the effective surface area) and also offer easy pathways for the electrolyte to reach every available surface.

3.2. Electrochemical Characterization: Effect of Redox Additive. The charge storage capacity of MnO_2 electrodes in aqueous KOH is based on two concurrent mechanisms: (i) surface adsorption or desorption of K^+ ions in the electrolyte on MnO_2 (nonfaradic current; see eq 8) and (ii) intercalation/deintercalation of K^+ ions into/from the nanostructured electrode material surface (faradic current; see eq 9) during reduction and oxidation, respectively.[49,50]

nonfaradic:

$$(MnO_2)_{surface} + K^+ + e^- \leftrightarrow (MnO_2K^+)_{surface} \quad (8)$$

faradic:

$$MnO_2 + K^+ + e^- \leftrightarrow MnO{\cdot}OK \quad (9)$$

The measured current is a combination of capacitor current (I_r), charging current (I_c), migration current (I_m), diffusion current (I_d), catalytic current (I_{cat}), and adsorption current ($I_{adsorop}$), but the major contribution comes from the diffusion current (I_d). Since most of the current components would be influenced by the concentration of the working electrolyte, we have first made a systematic investigation using different concentrations of KOH (Figure S2a, Supporting Information). It is observed that initially, with increasing concentration of KOH, the capacitance increases gradually up to 3 M KOH and then decreases with further increase in KOH concentration. However, following the general trend of transition metal oxide pseudocapacitors, with increasing scan rate, the specific capacitance value sharply decreases for all concentrations of KOH (Figure S2b, Supporting Information). Reversibility in CV can be achieved only if both the oxidant and reductant are stable and also if the kinetics of electron-transfer processes is fast enough so that, at all potential scan rates, the electron-transfer processes on the electrode/electrolyte interface are in Nernstian equilibrium. At a very slow scan rate the reversibility might hold, but with faster scan rates it may shift to being quasi-reversible or irreversible. In order to preserve the reversibility, the electron-transfer process must be accelerated and thus, we have introduced $K_4Fe(CN)_6$ as a redox-active electrolyte additive. But first, in order to evaluate the redox activities of the $Fe(CN)_6^{4-}/Fe(CN)_6^{3-}$ couple, cells were constructed with 3 M KOH + 0.1 M $K_3Fe(CN)_6$ and 3 M KOH + 0.1 M $K_4Fe(CN)_6$ as electrolytes using only bare Ni foils as electrodes as well as current collectors, and CV measurements were conducted at different scan rates ranging from 5 to 100 $mV \cdot s^{-1}$ (Figure S3, Supporting Information). For 3 M KOH + 0.1 M $K_3Fe(CN)_6$, a pair of sharp cathodic and anodic peaks are observed at E_{pc} = 0.06 V and E_{pa} = −0.06 V, corresponding to the redox reaction:

$$Fe(CN)_6^{3-} + e^- \leftrightarrow Fe(CN)_6^{4-} \quad (10)$$

These values are in good agreement with the reported peak potentials for the $Fe(CN)_6^{4-}/Fe(CN)_6^{3-}$ couple.[38] It was observed that, with continuous cycling at a particular scan rate, both I_{pc} and I_{pa} values gradually increase for the $K_4Fe(CN)_6$ system until an equilibrium is reached. This may be due to incomplete reversible reaction of $Fe(CN)_6^{4-}/Fe(CN)_6^{3-}$, that is, incomplete conversion of Fe(II) to Fe(III) and vice versa, because initially the system contains a large amount of Fe(II). This is validated by the observation of low I_{pc} and I_{pa} values in the CV of 3 M KOH + 0.1 M $K_4Fe(CN)_6$ (Figure S3, Supporting Information).

For evaluating the effect of of $K_4Fe(CN)_6$ as redox additive, CV measurements were conducted at six different scan rates ranging from 2 to 100 $mV \cdot s^{-1}$ with cells constructed with the developed α-MnO_2 electrodes using 3 M KOH and 3 M KOH + 0.1 M $K_4Fe(CN)_6$ as electrolytes in the potential window of −1 to +1 V (Figure 4a,b). Two interesting observations can be

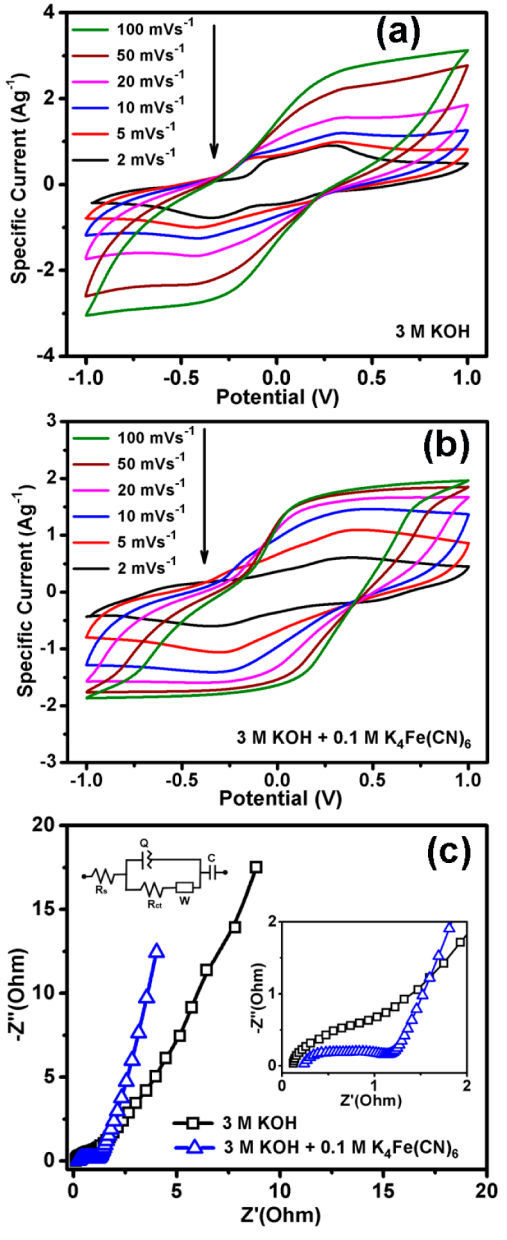

Figure 4. Electrochemical characterization of α-MnO_2 nanowire electrodes. (a, b) CV curves at different scan rates in (a) 3 M KOH or (b) 3 M KOH + 0.1 M $K_4Fe(CN)_6$ in the potential window of −1 to +1 V. (c) Nyquist plots. (Inset) Equivalent circuit used to fit impedance data.

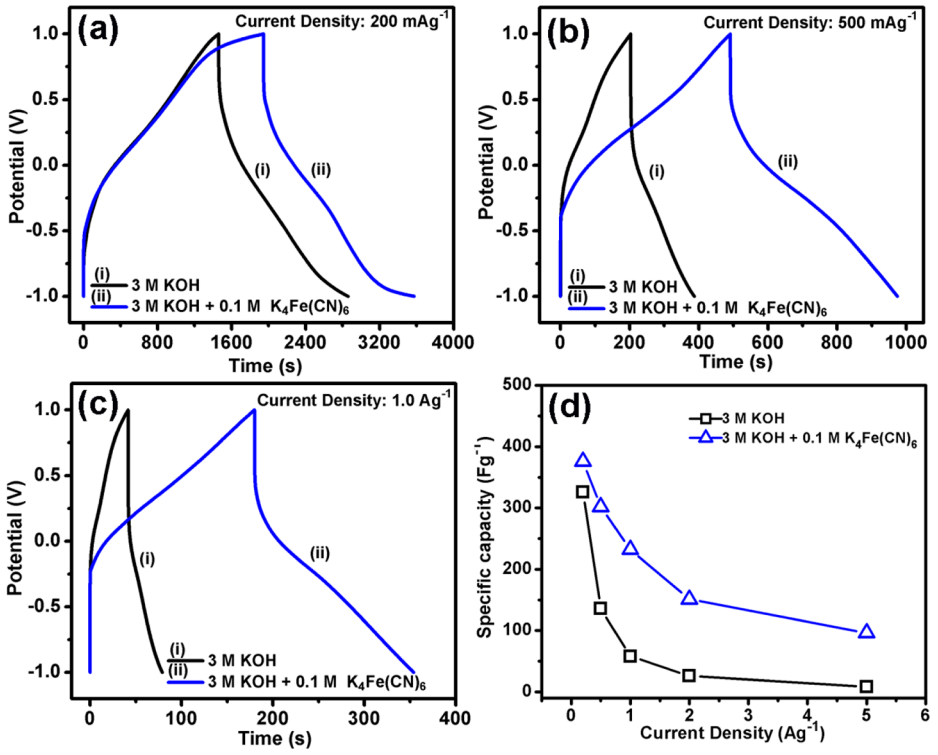

Figure 5. Electrochemical characterization of α-MnO_2 nanowire electrodes. (a–c) Galvanostatic charge–discharge profiles in 3 M KOH and 3 M KOH + 0.1 M $K_4Fe(CN)_6$ at different current densities: (a) 0.2, (b) 0.5, and (c) 1.0 $A{\cdot}g^{-1}$. (d) Variation of capacitance at different current densities in 3 M KOH and 3 M KOH + 0.1 M $K_4Fe(CN)_6$ in the potential window of −1 to +1 V.

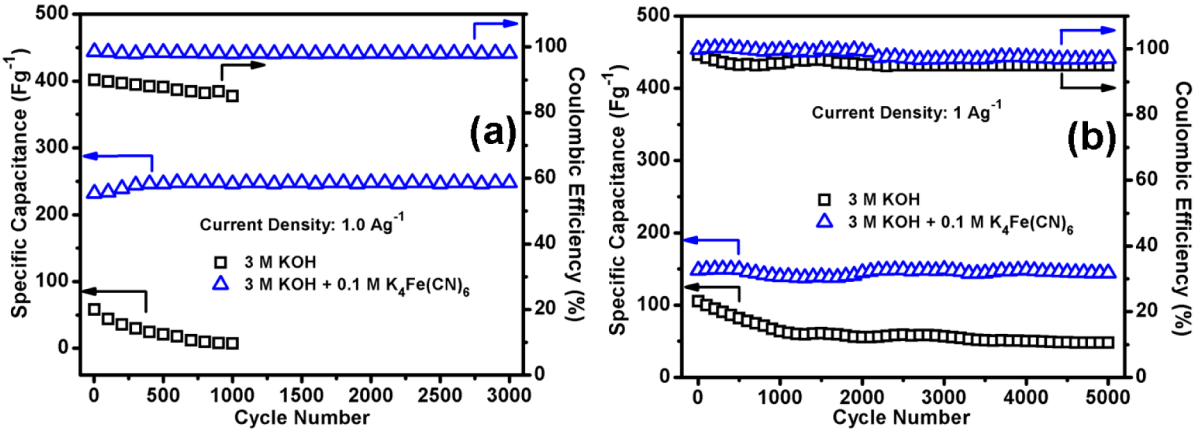

Figure 6. Electrochemical characterization of α-MnO_2 nanowire electrodes. Cycling behavior in 3 M KOH and 3 M KOH + 0.1 M $K_4Fe(CN)_6$ along with the respective Coulombic efficiencies in the potential window of (a) −1 to +1 V and (b) 0 to 1 V.

made when $Fe(CN)_6^{4-}$ is introduced as a redox additive to KOH: (i) Both cathodic and anodic processes appear to start earlier, that is, the difference in cathodic and anodic peak potentials tends to decrease. This may be due to the conjugation of two concurrent redox processes, Mn(IV)/Mn(III) and Fe(II)/Fe(III) as given in eqs 9 and 10, respectively. (ii) The shape of CV curves become more rectangular (i.e., toward better capacitive nature) with an overall increase in CV area. From the peak current of the CV plots (considering the flat portion of the cathodic scan), capacitance values of 775 and 622 $F{\cdot}g^{-1}$ are found for 3 M KOH and 3 M KOH + 0.1 M $K_4Fe(CN)_6$, respectively, at a scan rate of 2 $mV{\cdot}s^{-1}$. Electrochemical impedance spectroscopy measurements indicate that this decrease in the capacitance value in cells with $Fe(CN)_6^{4-}$ additive results from the slight increase in solution resistance (R_s). However, as seen from the Nyquist plots (Figure 4c), the spike observed in the low-frequency region becomes more vertical (i.e., more parallel to the y-axis) in the case of KOH with $K_4Fe(CN)_6$ additive, indicating superior capacitive behavior.[51] The results further indicate that conjugation of $Fe(CN)_6^{4-}/Fe(CN)_6^{3-}$ to Mn-(IV)/Mn(III) reduces the ionic diffusion resistance. Thus, at a higher scan rates, it is expected that the capacitance of the electrolytes with additive $K_4Fe(CN)_6$ will be higher. This indeed is found to be the case: even at 10 $mV{\cdot}s^{-1}$, the capacitance values are 250 and 286 $F{\cdot}g^{-1}$ for 3 M KOH and 3 M KOH + 0.1 M $K_4Fe(CN)_6$, respectively.

Since the discharge current in CV is not always constant across the entire potential window, often galvanostatic charge–discharge measurements are used for calculating the specific

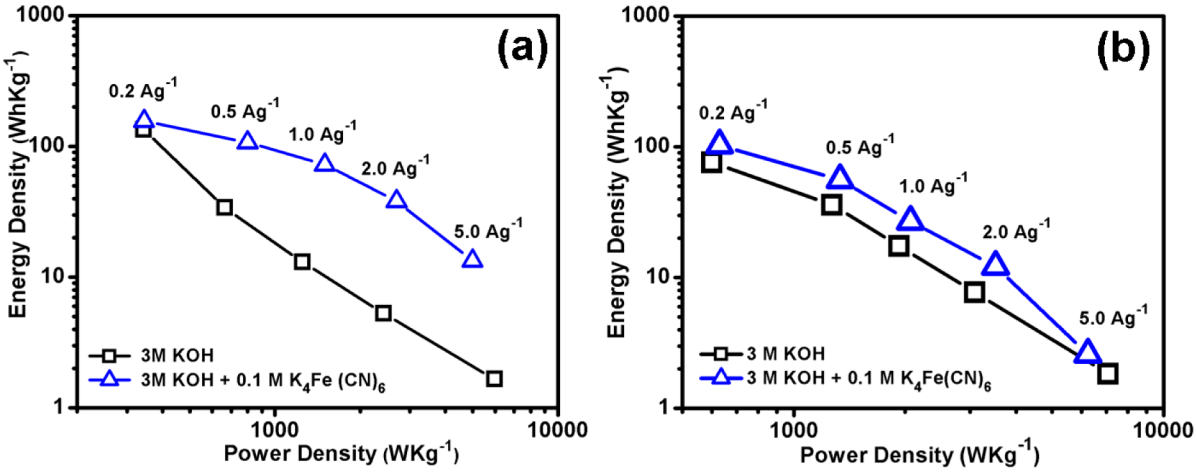

Figure 7. Electrochemical characterization of α-MnO_2 nanowire electrodes: Ragone plots for performance in 3 M KOH and 3 M KOH + 0.1 M $K_4Fe(CN)_6$ in the potential window of (a) −1 to +1 V and (b) 0 to 1 V.

capacitance of an electrode. A comparison of galvanostatic charge−discharge profiles (potential vs time) for 3 M KOH and 3 M KOH + 0.1 M $K_4Fe(CN)_6$ at different current densities of 0.2, 0.5, and 1 $A{\cdot}g^{-1}$ (Figure 5a−c, respectively) and also at 2 and 5 $A{\cdot}g^{-1}$ (Figure S4a,b, Supporting Information) clearly demonstrates the significant influence of redox additive on enhancement of reaction kinetics. Variation of capacitance with increasing current density is shown in Figure 5d. At a current density of 0.2 $A{\cdot}g^{-1}$, the observed capacitance values are 326 and 376 $F{\cdot}g^{-1}$ for 3 M KOH and 3 M KOH + 0.1 M $K_4Fe(CN)_6$, respectively. But as the current density is increased, a rapid capacitance fading is observed for 3 M KOH due the quasi-reversible redox reactions and a value of only 58 $F{\cdot}g^{-1}$ is found at a current density of 1 $A{\cdot}g^{-1}$. In the case of 3 M KOH + 0.1 M $K_4Fe(CN)_6$ as electrolyte, the corresponding capacitance value is 232 $F{\cdot}g^{-1}$ at 1 $A{\cdot}g^{-1}$, demonstrating a much higher rate capability. At a still higher current density of 5 $A{\cdot}g^{-1}$, the capacitance drops down to 8.3 $F{\cdot}g^{-1}$ (i.e., only 2.5% of the capacitance obtained at 0.2 $A{\cdot}g^{-1}$) for 3 M KOH, while the corresponding capacitance is 96 $F{\cdot}g^{-1}$ for 3 M KOH + 0.1 M $K_4Fe(CN)_6$ (i.e., 25.5% of the capacitance obtained at 0.2 $A{\cdot}g^{-1}$).

Cycling behavior of these symmetric cells has been tested in the potential window of −1 to +1 V at a current density of 1 $A{\cdot}g^{-1}$ for 1000 cycles in 3 M KOH and for 3000 cycles in 3 M KOH + 0.1 M $K_4Fe(CN)_6$ (Figure 6a). In 3 M KOH, a capacitance value of 58 $F{\cdot}g^{-1}$ is observed in the first cycle, which undergoes steady fading and only 13% of capacitance is retained at the 1000th cycle. On the other hand, in 3 M KOH + 0.1 M $K_4Fe(CN)_6$, the first cycle capacitance is 232 $F{\cdot}g^{-1}$. Interestingly, a gradual increase in capacitance can be observed up to around 200 cycles with a maximum capacitance value of 248 $F{\cdot}g^{-1}$, which is retained until the 3000th cycle with no apparent fading and with a high Coloumbic efficiency of 98%. In 3 M KOH + 0.1 M $K_4Fe(CN)_6$ as electrolyte, the redox reaction involved with the active material, that is, Mn(IV) ↔ Mn(III), is aided by the redox-active Fe(II) ↔ Fe(III) couple. Initially the system contains a large amount of Fe(II) that is oxidized to Fe(III) during charging, and during the discharging process Fe(III) is converted back to Fe(II). Upon continuous cycling, more and more Fe(II) is converted to Fe(III) and vice versa, until a time is reached when concentrations of both Fe(III) and Fe(II) become 0.05 M and an equilibrium is reached.[35] Thus, the $Fe(CN)_6^{4-}/Fe(CN)_6^{3-}$ redox system is actually working as an electron buffer source and this is manifested by observance of no further fading in capacitance once an equilibrium is established (Figure 6a).

Electrochemical performance of these symmetric cells has also been tested in the potential window of 0 to 1 V, and similar enhancement in the redox kinetics is observed upon addition of 0.1 M $K_4Fe(CN)_6$ into 3 M KOH electrolyte as depicted by the CV plots at different scan rates ranging from 2 to 100 $mV{\cdot}s^{-1}$ (Figure S5, Supporting Information) and the galvanostatic charge−discharge profiles at different current densities (Figure S6, Supporting Information). Figure 6b shows the cycling behavior in the potential window of 0 to 1 V at a current density of 1 $A{\cdot}g^{-1}$ for 5000 cycles in 3 M KOH and 3 M KOH + 0.1 M $K_4Fe(CN)_6$ as electrolytes. In 3 M KOH a capacitance value of 104 $F{\cdot}g^{-1}$ is observed in the first cycle, which undergoes steady fading, and only 46% of capacitance is retained at the 5000th cycle. On the other hand, in 3 M KOH + 0.1 M $K_4Fe(CN)_6$, the first-cycle capacitance is 149 $F{\cdot}g^{-1}$, 97% of which is retained until the 5000th cycle with a high Coloumbic efficiency of 99%, demonstrating the favorable effect of $K_4Fe(CN)_6$ redox additive on supercapacitor performance.

For a high-performance supercapacitor, a reasonably high energy density is required with a high power density. On the basis of the galvanostatic charge−discharge results at different current densities ranging from 0.2 to 5 $A{\cdot}g^{-1}$, the specific capacitance and energy and power densities of the cells were determined for both potential windows (i.e., −1 to +1 V and 0 to 1 V). In the Ragone plot for 3 M KOH and 3 M KOH + 0.1 M $K_4Fe(CN)_6$ in the potential window of −1 to +1 V (Figure 7a), it can be observed that, at a low current density of 0.2 $A{\cdot}g^{-1}$, the energy densities of both systems are nearly the same with high values of 344 and 345 $W{\cdot}h{\cdot}kg^{-1}$, respectively. However, as the current density is increased to 5 $A{\cdot}g^{-1}$, the energy density for 3 M KOH is reduced drastically to 1.7 $W{\cdot}h{\cdot}kg^{-1}$ with a corresponding power density of 5976 $W{\cdot}kg^{-1}$. On the other hand, for 3 M KOH + 0.1 M $K_4Fe(CN)_6$ system, the decrease in energy density is much slower with increasing current density. At 5 $A{\cdot}g^{-1}$, an energy density of 13 $W{\cdot}h{\cdot}kg^{-1}$ is obtained with the corresponding power density of 6500 $W{\cdot}kg^{-1}$. These values are superior to those reported earlier for MnO_2-based pseudocapacitors either in two-electrode[52−54] or

in three-electrode configuration.[55,56] As the Ragone plot in Figure 7b shows, in the potential window of 0 to 1 V, the energy densities are 76 and 103 $W{\cdot}h{\cdot}kg^{-1}$ at a current density of 0.2 $A{\cdot}g^{-1}$ for 3 M KOH and 3 M KOH + 0.1 M $K_4Fe(CN)_6$, respectively. That lower energy density values are obtained in the potential window of 0 to 1 V, in comparison to −1 to +1 V, may be due to incomplete redox processes involving partial conversion of Mn(IV) ↔ Mn(III).

4. CONCLUSIONS

In conclusion, we have demonstrated that combination of a simple two-way strategy—controlled morphology and addition of a redox-active couple to aqueous KOH—might be an effective way to alleviate the problem of the slow nature of faradic reactions in manganese dioxide-based pseudocapacitors. The presence of $Fe(CN)_6^{4-}/Fe(CN)_6^{3-}$ redox couple compensates for the slow nature of faradic reactions by providing an electron buffer source. These results may also stimulate the search for other redox-active electrolyte additives for improving the pseudocapacitive behavior of transition metal oxides.

■ ASSOCIATED CONTENT

Supporting Information

Six figures showing TGA curve for synthesized α-MnO_2 nanowires, CV curves of α-MnO_2 nanowire electrode in four KOH concentrations, variation of specific capacitance with increasing potential scan rate, CV curves at different scan rates of cells constructed with 3 M KOH + 0.1 M $K_3Fe(CN)_6$ or 3 M KOH + 0.1 M $K_4Fe(CN)_6$ as electrolyte using only bare Ni foils as electrodes as well as current collectors, CV curves at different scan rates in 3 M KOH and 3 M KOH + 0.1 M $K_4Fe(CN)_6$, and galvanostatic charge−discharge profiles at different current densities. This material is available free of charge via the Internet at http://pubs.acs.org/.

■ AUTHOR INFORMATION

Corresponding Author

*E-mail mahanty@cgcri.res.in or s_mahanty@hotmail.com; tel +91-33-23223495; fax +91-33-24730957.

Notes

The authors declare no competing financial interest.

■ ACKNOWLEDGMENTS

We thank the Director, CSIR-CGCRI, for kind permission to publish this work. Financial support from CSIR via TAPSUN NWP0056 project is gratefully acknowledged.

■ REFERENCES

(1) Winter, M.; Brodd, R. J. What are Batteries, Fuel Cells, and Supercapacitors. *Chem. Rev.* **2004**, *104*, 4245−4269.
(2) Conway, B. E. Electrochemical Science and Technology. *J. Electrochem. Soc.* **1991**, *138*, 1539−1548.
(3) Yan, J.; Fan, Z.; Wei, T.; Qian, W.; Zhang, M.; Wei, F. Fast and Reversible Surface Redox Reaction of Graphene-MnO_2 Composites as Supercapacitor Electrodes. *Carbon* **2010**, *48*, 3825−3833.
(4) Wang, X.; Wang, Y. Y.; Zhao, C. M.; Zhao, Y. X.; Yan, B. Y.; Zheng, W. T. Electrodeposited $Ni(OH)_2$ Nanoflakes on Graphite Nanosheets Prepared by Plasma-Enhanced Chemical Vapor Deposition for Supercapacitor Electrode. *New J. Chem.* **2012**, *36*, 1902−1906.
(5) Hastak, R. S.; Sivaraman, P.; Potphode, D. D.; Shashidhara, K.; Samui, A. B. All Solid Supercapacitor Based on Activated Carbon and Poly [2,5-Benzimidazole] for High Temperature Application. *Electrochim. Acta* **2012**, *59*, 296−303.
(6) Simon, P.; Gogotsi, Y. Materials for Electrochemical Capacitors. *Nat. Mater.* **2008**, *7*, 845−854.
(7) Toupin, M.; Brousse, T.; Belanger, D. Influence of Microstructure on the Charge Storage Properties of Chemically Synthesized Manganese Dioxide. *Chem. Mater.* **2002**, *14*, 3946−3952.
(8) Zhang, H.; Cao, G.; Wang, Z.; Yang, Y.; Shi, Z.; Gu, Z. Growth of Manganese Oxide Nanoflowers on Vertically-Aligned Carbon Nanotube Arrays for High-Rate Electrochemical Capacitive Energy Storage. *Nano Lett.* **2008**, *8*, 2664−2668.
(9) Chang, J. K.; Hsu, S. H.; Tsai, W. T.; Sun, I. W. A Novel Electrochemical Process to Prepare a High-Porosity Manganese Oxide Electrode with Promising Pseudocapacitive Performance. *J. Power Sources* **2008**, *177*, 676−680.
(10) Ma, S. B.; Nam, K. W.; Yoon, W. S.; Yang, X. Q.; Oh, K. H.; Kim, K. B. Electrochemical Properties of Manganese Oxide Coated onto Carbon Nanotubes for Energy-Storage Applications. *J. Power Sources* **2008**, *178*, 483−489.
(11) Beaudrouet, E.; La Salle, A. L. G.; Guyomard, D. Nanostructured Manganese Dioxides: Synthesis and Properties as Supercapacitor Electrode Materials. *Electrochim. Acta* **2009**, *54*, 1240−1248.
(12) Jiang, H.; Zhao, T.; Ma, J.; Yan, C.; Li, C. Z. Ultrafine Manganese Dioxide Nanowire Network for High-Performance Supercapacitors. *Chem. Commun.* **2011**, *47*, 1264−1266.
(13) Sung, D. Y.; Kim, I. Y.; Kim, T. W.; Song, M. S.; Hwang, S. J. Room Temperature Synthesis Routes to the 2D Nanoplates and 1D Nanowires/Nanorods of Manganese Oxides with Highly Stable Pseudocapacitance Behaviors. *J. Phys. Chem. C* **2011**, *115*, 13171−13179.
(14) Zhang, J. T.; Chu, W.; Jiang, J. W.; Zhao, X. S. Synthesis, Characterization and Capacitive Performance of Hydrous Manganese Dioxide Nanostructures. *Nanotechnology* **2011**, *22*, No. 125703.
(15) Song, M. S.; Lee, K. M.; Lee, Y. R.; Kim, T. W.; Hwang, S. J. Porously Assembled 2D Nanosheets of Alkali Metal Manganese Oxides with Highly Reversible Pseudocapacitance Behaviors. *J. Phys. Chem. C* **2010**, *114*, 22134−22140.
(16) Portehault, D.; Cassaignon, S.; Nassif, N.; Baudrin, E.; Jolivet, J. P. A Core-Corona Hierarchical Manganese Oxide and its Formation by an Aqueous Soft Chemistry Mechanism. *Angew. Chem., Int. Ed.* **2008**, *47*, 6441−6444.
(17) Zhang, Z. Q.; Mu, J. Hydrothermal Synthesis of γ-MnOOH Nanowires and α-MnO_2 Sea Urchin-Like Clusters. *Solid State Commun.* **2007**, *141*, 427−430.
(18) Yuan, J. K.; Li, W. N.; Sinue, G.; Steven, L. Shape-Controlled Synthesis of Manganese Oxide Octahedral Molecular Sieve Three-Dimensional Nanostructures. *J. Am. Chem. Soc.* **2005**, *127*, 14184−14185.
(19) Deng, S.; Sun, D.; Wu, C. H.; Wang, H.; Liu, J. B.; Sun, Y. X.; Yan, H. Synthesis and Electrochemical Properties of MnO_2 Nanorods/Graphene Composites for Supercapacitor Applications. *Electrochim. Acta* **2013**, *111*, 707−712.
(20) Gao, H.; Xiao, F.; Ching, C. B.; Duan, H. High-Performance Asymmetric Supercapacitor Based on Graphene Hydrogel and Nanostructured MnO_2. *ACS Appl. Mater. Interfaces* **2012**, *4*, 2801−2810.
(21) Yu, G.; Hu, L.; Liu, N.; Wang, H.; Vosgueritchian, M.; Yang, Y.; Cui, Y.; Bao, Z. Enhancing the Supercapacitor Performance of Graphene/MnO_2 Nanostructured Electrodes by Conductive Wrapping. *Nano Lett.* **2011**, *11*, 4438−4442.
(22) Yu, G.; Hu, L.; Vosgueritchian, M.; Wang, H.; Xie, X.; McDonough, J. R.; Cui, X.; Cui, Y.; Bao, Z. Solution-Processed Graphene/MnO_2 Nanostructured Textiles for High-Performance Electrochemical Capacitors. *Nano Lett.* **2011**, *11*, 2905−2911.
(23) Yang, S.; Song, X.; Zhang, P.; Gao, L. Facile Synthesis of Nitrogen-Doped Graphene-Ultrathin MnO_2 Sheet Composites and Their Electrochemical Performances. *ACS Appl. Mater. Interfaces* **2013**, *5*, 3317−3322.

(24) Li, Q.; Lu, X.-F.; Xu, H.; Tong, Y.-X.; Li, G.-R. Carbon/MnO_2 Double-Walled Nanotube Arrays with Fast Ion and Electron Transmission for High-Performance Supercapacitors. *ACS Appl. Mater. Interfaces* **2014**, *6*, 2726−2733.
(25) Reddy, A. L. M.; Shaijumon, M. M.; Gowda, S. R.; Ajayan, P. M. Multisegmented Au-MnO_2/Carbon Nanotube Hybrid Coaxial Arrays for High-Power Supercapacitor Applications. *J. Phys. Chem. C* **2010**, *114*, 658−663.
(26) Chen, W.; Rakhi, R. B.; Hu, L.; Xie, X.; Cui, Y.; Alshareef, H. N. High-Performance Nanostructured Supercapacitors on a Sponge. *Nano Lett.* **2011**, *11*, 5165−5172.
(27) Sumboja, A.; Foo, C. Y.; Yan, J.; Yan, C.; Gupta, R. K.; Lee, P. S. Significant Electrochemical Stability of Manganese Dioxide/Polyaniline Coaxial Nanowires by Self-Terminated Double Surfactant Polymerization for Pseudocapacitor Electrode. *J. Mater. Chem.* **2012**, *22*, 23921−23928.
(28) Ranjusha, R.; Sajesh, K. M.; Roshny, S.; Lakshmi, V.; Anjali, P.; Sonia, T. S.; Nair, A. S.; Subramanian, K. R. V.; Nair, S. V.; Chennazhi, K. P.; Balakrishnan, A. Supercapacitors Based on Freeze Dried MnO_2 Embedded PEDOT:PSS Hybrid Sponges. *Microporous Mesoporous Mater.* **2014**, *186*, 30−36.
(29) Liu, M.; Gan, L.; Xiong, W.; Xu, Z.; Zhu, D.; Chen, L. Development of MnO_2/Porous Carbon Microspheres with a Partially Graphitic Structure for High Performance Supercapacitor Electrodes. *J. Mater. Chem. A* **2014**, *2*, 2555−2562.
(30) Lu, X.; Yu, M.; Wang, G.; Zhai, T.; Xie, S.; Ling, Y.; Tong, Y.; Li, Y. H-TiO_2@MnO_2//H-TiO_2@C Core-Shell Nanowires for High Performance and Flexible Asymmetric Supercapacitors. *Adv. Mater.* **2013**, *25*, 267−272.
(31) Yang, P.; Xiao, X.; Li, Y.; Ding, Y.; Qiang, P.; Tan, X.; Mai, W.; Lin, Z.; Wu, W.; Li, T.; Jin, H.; Liu, P.; Zhou, J.; Wong, C. P.; Wang, Z. L. Hydrogenated ZnO Core-Shell Nanocables for Flexible Supercapacitors and Self-Powered Systems. *ACS Nano* **2013**, *7*, 2617−2626.
(32) Li, Q.; Wang, Z. L.; Li, G. R.; Guo, R.; Ding, L. X.; Tong, Y. X. Design and Synthesis of MnO_2/Mn/MnO_2 Sandwich-Structured Nanotube Arrays with High Supercapacitive Performance for Electrochemical Energy Storage. *Nano Lett.* **2012**, *12*, 3803−3807.
(33) Zhang, G.; Zheng, L.; Zhang, M.; Guo, S.; Liu, Z. H.; Yang, Z.; Wang, Z. Preparation of Ag-Nanoparticle-Loaded MnO_2 Nanosheets and Their Capacitance Behavior. *Energy Fuels* **2012**, *26*, 618−623.
(34) Ma, J.; Cheng, Q.; Pavlinek, V.; Saha, P.; Li, C. Morphology-Controllable Synthesis of MnO_2 Hollow Nanospheres and Their Supercapacitive Performance. *New J. Chem.* **2013**, *37*, 722−728.
(35) Wang, H.-Q.; Yang, G.-F.; Li, Q.-Y.; Zhong, X.-X.; Wang, F.-P.; Li, Z.-S.; Li, Y.-H. Porous Nano-MnO_2: Large Scale Synthesis Via a Facile Quick-Redox Procedure and Application in a Supercapacitor. *New J. Chem.* **2011**, *35*, 469−475.
(36) Xia, X.; Chao, D.; Fan, Z.; Guan, C.; Cao, X.; Zhang, H.; Fan, H. J. A New Type of Porous Graphite Foams and Their Integrated Composites with Oxide/Polymer Core/Shell Nanowires for Supercapacitors: Structural Design, Fabrication, and Full Supercapacitor Demonstrations. *Nano Lett.* **2014**, *14*, 1651−1658.
(37) Su, L. H.; Zhang, X. G.; Mi, C. H.; Gao, B.; Liu, Y. Improvement of the Capacitive Performances for Co-Al Layered Double Hydroxide by Adding Hexacyanoferrate into the Electrolyte. *Phys. Chem. Chem. Phys.* **2009**, *11*, 2195−2202.
(38) Zhao, C.; Zheng, W.; Wang, X.; Zhang, H.; Cui, X.; Wang, H. Ultrahigh Capacitive Performance from both $Co(OH)_2$/Graphene Electrode and $K_3Fe(CN)_6$ Electrolyte. *Sci. Rep.* **2013**, *3*, 2986.
(39) Pandolfo, A. G.; Hollenkamp, A. F. Carbon Properties and Their Role in Supercapacitors. *J. Power Sources* **2006**, *157*, 11−27.
(40) Wang, G.; Zhang, L.; Zhang, J. A Review of Electrode Materials for Electrochemical Supercapacitors. *Chem. Soc. Rev.* **2012**, *41*, 797−828.
(41) Meng, Y.; Wang, K.; Zhang, Y.; Wei, Z. Hierarchical Porous Graphene/Polyaniline Composite Film with Superior Rate Performance for Flexible Supercapacitors. *Adv. Mater.* **2013**, *25*, 6985−6990.
(42) Ghaffari, M.; Zhou, Y.; Xu, H.; Lin, M.; Kim, T. Y.; Ruoff, R. S.; Zhang, Q. M. High-Volumetric Performance Aligned Nano-Porous Microwave Exfoliated Graphite Oxide-based Electrochemical Capacitors. *Adv. Mater.* **2013**, *25*, 4879−4885.
(43) Julien, C. M.; Massot, M.; Poinsignon, C. Lattice Vibrations of Manganese Oxides: Part I. Periodic Structures. *Spectrochim. Acta, Part A* **2004**, *60*, 689−700.
(44) Zhang, L. C.; Liu, Z. H.; Tang, X. H.; Wang, J. F.; Ooi, K. Synthesis and Characterization of β-MnO_2 Single Crystals with Novel Tetragonous Morphology. *Mater. Res. Bull.* **2007**, *42*, 1432−1439.
(45) Jana, S.; Pande, S.; Sinha, A. K.; Sarkar, S.; Pradhan, M.; Basu, M.; Saha, S.; Pal, T. A Green Chemistry Approach for the Synthesis of Flower-Like Ag-Doped MnO_2 Nanostructures Probed by Surface-Enhanced Raman Spectroscopy. *J. Phys. Chem. C* **2009**, *113*, 1386−1392.
(46) Sinha, A. K.; Pradhan, M.; Pal, T. Morphological Evolution of Two-Dimensional MnO_2 Nanosheets and Their Shape Transformation to One-Dimensional Ultralong MnO_2 Nanowires for Robust Catalytic Activity. *J. Phys. Chem. C* **2013**, *117*, 23976−23986.
(47) Sung, D.-Y.; Kim, I. Y.; Kim, T. W.; Song, M.-S.; Hwang, S.-J. Room Temperature Synthesis Routes to the 2D Nanoplates and 1D Nanowires/Nanorods of Manganese Oxides with Highly Stable Pseudocapacitance Behaviors. *J. Phys. Chem. C* **2011**, *115*, 13171−13179.
(48) Wei, W.; Cui, X.; Chen, W.; Ivey, D. G. Manganese Oxide-Based Materials as Electrochemical Supercapacitor Electrodes. *Chem. Soc. Rev.* **2011**, *40*, 1697−1721.
(49) Subramanian, V.; Zhu, H.; Wei, B. Nanostructured MnO_2: Hydrothermal Synthesis and Electrochemical Properties as a Supercapacitor Electrode Material. *J. Power Sources* **2006**, *159*, 361−364.
(50) Toupin, M.; Brousse, T.; Belanger, D. Charge Storage Mechanism of MnO_2 Electrode Used in Aqueous Electrochemical Capacitor. *Chem. Mater.* **2004**, *16*, 3184−3190.
(51) Fan, Z. J.; Yan, J.; Wei, T.; Zhi, L. J.; Ning, G. Q.; Li, T. Y.; Wei, F. Asymmetric Supercapacitors Based on Graphene/MnO_2 and Activated Carbon Nanofiber Electrodes with High Power and Energy Density. *Adv. Funct. Mater.* **2011**, *21*, 2366−2375.
(52) He, Y.; Chen, W.; Li, X.; Zhang, Z.; Fu, J.; Zhao, C.; Xie, E. Freestanding Three-Dimensional Graphene/MnO_2 Composite Networks as Ultralight and Flexible Supercapacitor Electrodes. *ACS Nano* **2013**, *7*, 174−182.
(53) Wang, J.-G.; Yang, Y.; Huang, Z.-H.; Kang, F. A High-Performance Asymmetric Supercapacitor Based on Carbon and Carbon-MnO_2 Nanofiber Electrodes. *Carbon* **2013**, *61*, 190−199.
(54) Wu, Z.-S.; Ren, W.; Wang, D.-W.; Li, F.; Liu, B.; Cheng, H.-M. High-Energy MnO_2 Nanowire/Graphene and Graphene Asymmetric Electrochemical Capacitors. *ACS Nano* **2010**, *4*, 5835−5842.
(55) Yuan, L.; Lu, X.-H.; Xiao, X.; Zhai, T.; Dai, J.; Zhang, F.; Hu, B.; Wang, X.; Gong, L.; Chen, J.; Hu, C.; Tong, Y.; Zhou, J.; Wang, Z. L. Flexible Solid-State Supercapacitors Based on Carbon Nanoparticles/MnO_2 Nanorods Hybrid Structure. *ACS Nano* **2012**, *6*, 656−661.
(56) Jin, Y.; Chen, H.; Chen, M.; Liu, N.; Li, Q. Graphene-Patched CNT/MnO_2 Nanocomposite Papers for the Electrode of High-Performance Flexible Asymmetric Supercapacitors. *ACS Appl. Mater. Interfaces* **2013**, *5*, 3408−3416.